

A lattice Boltzmann method for binary fluids based on mass-conserved quasi-incompressible phase-field theory

Kang Yang and Zhaoli Guo*

State Key Laboratory of Coal Combustion,

Huazhong University of Science and Technology, Wuhan 430074, China

(Dated: September 2, 2018)

Abstract

In this paper, a lattice Boltzmann equation (LBE) model is proposed for binary fluids based on a quasi-incompressible phase-field model [J. Shen et al, *Comm. Comp. Phys.* 13, 1045 (2013)]. Compared with the other incompressible LBE models based on the incompressible phase-field theory, the quasi-incompressible model conserves mass locally. A series of numerical simulations are performed to validate the proposed model, and comparisons with an incompressible LBE model [H. Liang et al, *Phys. Rev. E* 89, 053320 (2014)] are also carried out. It is shown that the proposed model can track the interface accurately, and the predictions by the quasi-incompressible and incompressible models agree qualitatively well as the distribution of chemical potential is uniform, otherwise differ significantly.

PACS numbers: 02.70.-c, 47.11.-j, 47.55.-t

* zlguo@hust.edu.cn

I. INTRODUCTION

Multiphase fluid flows are ubiquitous in engineering problems and natural processes. Generally, a phase interface can be described by sharp interface approach [1–3] or diffuse interface approach [4–11]. In the sharp interface approach, the fluid is separated into some sub-domains by sharp interfaces in which each sub-domain contains only one phase, and the fluid properties such as density and viscosity are discontinuous across the interfaces. On the contrary, in diffuse interface approach, the fluid is treated continuously in the whole domain and the fluid properties vary smoothly across interfaces. An attractive feature of the diffuse interface method is it can model the complex interfacial dynamics without explicitly tracking the interfaces, and this feature makes it an ideal basis for developing efficient numerical schemes.

In the diffuse interface approach, usually a phase-field variable (or order parameter) is used to distinguish different phases. The variable takes two distinct constant values in the bulk regions of the two phases, respectively, and changes smoothly across the interface. Based on the phase-field variable and its gradient, the free-energy of the system can be modelled, from which one can obtain a transport equation for the order parameter. The dynamic change of the phase interface can then be described by this equation coupled with the governing equations of the flow. In most of previous works on immiscible binary mixtures of incompressible fluids, the flow is usually assumed to be governed by the incompressible Navier-Stokes equations including the interfacial force. However, as pointed out in [8], the assumption that the mixture is incompressible in the whole region is inconsistent with the conservation of mass as the densities of the fluids are unequal. To remedy this physical problem, a quasi-incompressible phase-field model, which assumes the mixture is incompressible in bulk regions but compressible in the mixing layer, has been proposed [7].

A number of numerical schemes have been developed based on phase-field models including spectral methods [4, 12, 13], finite element methods [14–16] and LBE methods [9–11]. Among these methods, the LBE method has received particular attentions due to some distinctive features [19]. The first phase-field LBE model was proposed by He *et al.* [9] which adopts an order parameter to track the interface of two incompressible fluids. However, there exist some differences between the derived governing equations and the phase-field theory for incompressible two-phase flows [23, 26], and numerical instability can be produced for systems with a large density ratio. Later some improved LBE models based on phase-field

theory have been developed from different viewpoints. For instance, in order to improve numerical stability, Lee and Lin [11] designed a three-stage discretization multiphase lattice Boltzmann (LB) scheme by discretizing the gradient terms in different manners before and after the streaming step. Later, Fakhari *et al.* [21] further generalized the model [11] by employing a multi-relaxation-time collision operator. Zheng [10] and Zu [23] respectively proposed the modified LBE models in order to recover the correct Cahn-Hilliard (CH) equation. However, the extra terms in the both models will produce a large error in the interface capturing and the computation will become unstable as the dimensionless relaxation time equals to 1[23]. To overcome these problems, Liang *et al.* [24] proposed a new LBE model by introducing a time-dependent source term in the evolution equation. Recently, Zheng *et al.* [25] presented an alternative model based on the kinetic theory to solve the problem. Although those LBE models [10, 23, 25] could recover the CH equation exactly, the recovered momentum equations are still inconsistent with the target momentum equations for the incompressible flows. Li *et al.* [26] noted this problem and proposed a correction method by introducing an artificial interfacial force.

All of the above LBE models were developed based on the incompressible phase-field models that do not conserve mass locally as the two fluids have different densities. In this work we aim to develop a LBE model based on the quasi-incompressible phase-field theory for two-phase flows, which can ensure the exact mass conservation. The rest of this paper is organized as follows. In Sec. 2, the quasi-incompressible phase field model is briefly reviewed, and a LBE model based on this theory is constructed in Sec. 3. In Sec. 4, some numerical simulations are carried out to validate the proposed model, and some comparisons with a recent incompressible LBE model are also made. A brief summary is presented in section 5.

II. QUASI-INCOMPRESSIBLE PHASE-FIELD MODEL

In the phase field theory for a two-phase system, the thermodynamic behavior can be described by a free energy function with respect to an order parameter ϕ

$$F(\phi) = \int_{\Omega} [\psi(\phi) + \frac{\kappa}{2} |\nabla \phi|^2] d\Omega, \quad (1)$$

where ϕ is used to distinguish different phases, $\psi(\phi)$ is the bulk free-energy density, κ is the coefficient of surface tension, and Ω is the control volume.

For binary fluids, a double-well form of free-energy density [5, 28] can be used

$$\psi(\phi) = \beta(\phi - \phi_A)^2(\phi - \phi_B)^2, \quad (2)$$

where ϕ_A and ϕ_B are the equilibrium values of the order parameters for fluids A and B, respectively, β is a constant related to the interfacial thickness W [5, 28, 29] and the surface tension σ [29, 30],

$$W = \frac{1}{|\phi_A - \phi_B|} \sqrt{\frac{8\kappa}{\beta}}, \quad (3)$$

and

$$\sigma = \frac{|\phi_A - \phi_B|^3}{6} \sqrt{2\kappa\beta}. \quad (4)$$

With the bulk free energy, the chemical potential μ [5, 28, 29] can be obtained

$$\begin{aligned} \mu &= \frac{\delta F}{\delta \phi} = \frac{\partial \psi}{\partial \phi} - \kappa \nabla^2 \phi \\ &= 4\beta(\phi - \phi_A)(\phi - \phi_B)\left(\phi - \frac{\phi_A + \phi_B}{2}\right) - \kappa \nabla^2 \phi, \end{aligned} \quad (5)$$

and the order-parameter profile across the equilibrium interface can be obtained by solving $\mu(\phi) = 0$ [29],

$$\phi(\zeta) = \frac{\phi_A + \phi_B}{2} + \frac{\phi_A - \phi_B}{2} \tanh\left(\frac{2\zeta}{W}\right), \quad (6)$$

where ζ is the coordinate normal to the interface. The evolution of the order parameter can be described by the Cahn-Hilliard (CH) equation [5, 28, 31, 32]

$$\frac{\partial \phi}{\partial t} + \nabla \cdot (\phi \mathbf{u}) = \nabla \cdot (\lambda \nabla \mu), \quad (7)$$

where λ is the mobility coefficient and \mathbf{u} is the fluid velocity.

In the incompressible phase-field model, the fluid is assumed to be incompressible everywhere, and the flow can be described by the incompressible Navier-Stokes equations with an interfacial force [6, 33],

$$\frac{\partial \phi}{\partial t} + \nabla \cdot (\phi \mathbf{u}) = \nabla \cdot (\lambda \nabla \mu), \quad (8)$$

$$\rho \left(\frac{\partial \mathbf{u}}{\partial t} + \mathbf{u} \cdot \nabla \mathbf{u} \right) = -\nabla p + \nabla \cdot [\rho \nu (\nabla \mathbf{u} + \nabla \mathbf{u}^T)] + \mathbf{F}, \quad (9)$$

$$\nabla \cdot \mathbf{u} = 0, \quad (10)$$

with

$$\rho = \frac{\phi - \phi_B}{\phi_A - \phi_B} (\rho_A - \rho_B) + \rho_B, \quad (11)$$

where ρ_A and ρ_B are the densities of fluids A and B, respectively. From Eqs. (8), (10) and (11), we can obtain

$$\frac{\partial \rho}{\partial t} + \nabla \cdot (\rho \mathbf{u}) = \frac{d\rho}{d\phi} \nabla \cdot [\lambda \nabla \mu], \quad (12)$$

where

$$\frac{d\rho}{d\phi} = \frac{\rho_A - \rho_B}{\phi_A - \phi_B}. \quad (13)$$

It is obvious that the mass conservation is constrained by the $d\rho/d\phi$ and $\nabla \cdot [\lambda \nabla \mu]$. In generally, $\nabla \cdot [\lambda \nabla \mu]$ is nonzero in the interfacial region. Hence, as long as $\rho_A \neq \rho_B$, the mass is not locally conserved in the incompressible phase-field model.

In the quasi-incompressible phase field model [27], the governing equations are expressed as

$$\frac{\partial \phi}{\partial t} + \nabla \cdot (\phi \mathbf{u}) = \nabla \cdot (\lambda \nabla \mu), \quad (14)$$

$$\rho \left(\frac{\partial \mathbf{u}}{\partial t} + \mathbf{u} \cdot \nabla \mathbf{u} \right) = -\nabla p + \nabla \cdot [\rho \nu (\nabla \mathbf{u} + \nabla \mathbf{u}^T)] + \mathbf{F}, \quad (15)$$

$$\nabla \cdot \mathbf{u} = -\gamma \nabla \cdot [\lambda \nabla \mu], \quad (16)$$

with

$$\gamma = \frac{d\rho/d\phi}{\rho - \phi d\rho/d\phi} = \frac{\rho_r - 1}{\phi_A - \phi_B \rho_r}, \quad (17)$$

where p is the hydrodynamic pressure, ν is the kinematic viscosity, \mathbf{F} is the total force including the surface tension force $\mathbf{F}_s (= -\phi \nabla \mu)$ and other body forces \mathbf{F}_b , ρ_r is the density ratio ρ_A/ρ_B . From Eqs. (12), (15) and (16), one can obtain that

$$\partial_t \rho + \nabla \cdot (\rho \mathbf{u}) = 0, \quad (18)$$

which means that the mass is conserved locally in the quasi-incompressible model. Furthermore, equation (16) suggests that the fluid is compressible in the mixing zone. To investigate the effect of compressibility, we substitute Eq. (16) into Eq. (14) to get,

$$\frac{\partial \phi}{\partial t} + \mathbf{u} \cdot \nabla \phi = (1 + \gamma \phi) \nabla \cdot (\lambda \nabla \mu). \quad (19)$$

On the other hand, from Eqs. (8) and (10) we can obtain

$$\frac{\partial \phi}{\partial t} + \mathbf{u} \cdot \nabla \phi = \nabla \cdot (\lambda \nabla \mu). \quad (20)$$

From Eqs. (19) and (20), we can see that the discrepancy between the two models is related to the term $\gamma \phi \nabla \cdot (\lambda \nabla \mu)$, which depends on the density ratio and the spatial distribution of the chemical potential. If the chemical potential is uniformly distributed, the additional

term plays weak role in the results, otherwise the discrepancy between the two models is tremendous. Eq. (19) can be also expressed in dimensionless formulation as

$$\begin{aligned} \partial_t \phi + \mathbf{u} \cdot \nabla \phi &= (1 + \gamma \phi) P e^{-1} \nabla^2 \{4(\phi - \phi_A)(\phi - \phi_B)[\phi - (\phi_A + \phi_B)/2] \\ &\quad - C n^2 (\phi_A - \phi_B)^2 \nabla^2 \phi / 8\}, \end{aligned} \quad (21)$$

where $Pe = U_c L_c / \lambda \beta$ is the Peclet number and $Cn = W / L_c$ is the Cahn number with the characteristic length L_c and velocity U_c . This suggests that the distinctions between the two models are also related to the magnitudes of Pe and Cn . In the numerical simulations, we will investigate the difference between the two models by changing the dimensionless parameters Pe , Cn and γ .

III. THE QUASI-INCOMPRESSIBLE LBE MODEL

In this section, we will propose the LBE model based on the quasi-incompressible phase-field equations [27]. The model consists of two LBEs, one for the CH equation, and one for the Navier-Stokes equations,

$$f_i(\mathbf{x} + \mathbf{c}_i \delta t, t + \delta t) - f_i(\mathbf{x}, t) = -\frac{1}{\tau_f} [f_i(\mathbf{x}, t) - f_i^{eq}(\mathbf{x}, t)] + \delta t \left[1 - \frac{1}{2\tau_f}\right] F_i, \quad (22)$$

$$g_i(\mathbf{x} + \mathbf{c}_i \delta t, t + \delta t) - g_i(\mathbf{x}, t) = -\frac{1}{\tau_g} [g_i(\mathbf{x}, t) - g_i^{eq}(\mathbf{x}, t)] + \delta t \left[1 - \frac{1}{2\tau_g}\right] G_i, \quad (23)$$

where $f_i(\mathbf{x}, t)$ and $g_i(\mathbf{x}, t)$ are the distribution functions for the hydrodynamics and order parameter fields, respectively, \mathbf{c}_i is the discrete velocity in the i th direction, δt is the time step, τ_f and τ_g are dimensionless relaxation times related to the shear viscosity and mobility, respectively, F_i and G_i are the distribution functions for the force term, and G_i is used for eliminating the extra term in the CH equation [34]. The local equilibrium distribution functions $f_i^{eq}(\mathbf{x}, t)$ and $g_i^{eq}(\mathbf{x}, t)$ are respectively defined as

$$f_i^{eq} = \omega_i [p + c_s^2 \rho s_i(\mathbf{u})], \quad (24)$$

$$g_i^{eq} = H_i + \omega_i \phi s_i(\mathbf{u}), \quad (25)$$

with

$$s_i(\mathbf{u}) = \frac{\mathbf{c}_i \cdot \mathbf{u}}{c_s^2} + \frac{\mathbf{u} \mathbf{u} : (\mathbf{c}_i \mathbf{c}_i - c_s^2 \mathbf{I})}{2c_s^4}, \quad (26)$$

$$H_i = \begin{cases} \phi - (1 - \omega_0)\alpha\mu, & i = 0 \\ \omega_i\alpha\mu, & i \neq 0 \end{cases} \quad (27)$$

where ω_i is the weighting coefficient, D is the spatial dimension and c_s is the sound speed for an ideal fluid, and α is an adjustable parameter for a given mobility.

In Eqs. (22) and (23), the source terms F_i and G_i are respectively given by

$$F_i = (\mathbf{c}_i - \mathbf{u}) \cdot [\omega_i \mathbf{F} \Gamma_i(\mathbf{u}) + \omega_i s_i(\mathbf{u}) c_s^2 \nabla \rho] - \omega_i c_s^2 \rho \gamma \nabla \cdot (\lambda \nabla \mu), \quad (28)$$

$$G_i = -\frac{\phi}{c_s^2 \rho} (\mathbf{c}_i - \mathbf{u}) \cdot (\nabla p - \mathbf{F}) \omega_i \Gamma_i(\mathbf{u}). \quad (29)$$

The macroscopic quantities, ϕ , \mathbf{u} and p , are computed evaluated as

$$\phi = \sum_i g_i, \quad (30)$$

$$\mathbf{u} = \frac{1}{c_s^2 \rho} \left[\sum_i \mathbf{c}_i f_i + \frac{\delta t}{2} c_s^2 \mathbf{F} \right], \quad (31)$$

$$p = \sum_i f_i + \frac{\delta t}{2} c_s^2 (\mathbf{u} \cdot \nabla \rho - \gamma \rho \nabla \cdot (\lambda \nabla \mu)). \quad (32)$$

The kinetic viscosity ν and the mobility λ are respectively given by

$$\nu = c_s^2 (\tau_f - 0.5) \delta t, \quad \lambda = c_s^2 (\tau_g - 0.5) \alpha \delta t. \quad (33)$$

Through the Chapman-Enskog analysis (see the Appendix for details), we can obtain the following macroscopic hydrodynamics equations

$$\rho \left(\frac{\partial \mathbf{u}}{\partial t} + \mathbf{u} \cdot \nabla \mathbf{u} \right) = -\nabla p + \nabla \cdot [\rho \nu (\nabla \mathbf{u} + \nabla \mathbf{u}^T)] + \mathbf{F}, \quad (34)$$

$$\frac{1}{c_s^2 \rho} \frac{\partial p}{\partial t} + \nabla \cdot \mathbf{u} = -\gamma \nabla \cdot [\lambda \nabla \mu], \quad (35)$$

$$\frac{\partial \phi}{\partial t} + \nabla \cdot (\phi \mathbf{u}) = \nabla \cdot (\lambda \nabla \mu). \quad (36)$$

In the limit of low Mach number ($Ma = |\mathbf{u}|/c_s$), the dynamic pressure is assumed to be $p \sim O(Ma^2)$, and the above set of equations reduce to quasi-incompressible model given by Eqs. (14) to (16).

In the present work, we consider two-dimensional cases, and the two-dimensional nine-velocity (D2Q9) LBE model is used without loss of generality, in which $\mathbf{c}_0 = (0, 0)$, $\mathbf{c}_{i=1-4} = c\{\cos[(i-1)\pi/2], \sin[(i-1)\pi/2]\}$, $\mathbf{c}_{i=5-8} = \sqrt{2}c\{\cos[(2i-1)\pi/4], \sin[(2i-1)\pi/4]\}$, and the corresponding weight coefficients are $\omega_0 = 4/9$, $\omega_{1-4} = 1/9$ and $\omega_{5-8} = 1/36$. The sound

speed c_s is given by $c_s = c/\sqrt{3}$, where $c = \delta x/\delta t$, with δx representing the lattice space. For simplicity, we set the lattice space and time increment as the length and time units, i.e., $\delta x = \delta t = 1$. In the computations, the gradient operators are discretized with the isotropic central scheme [35].

IV. NUMERICAL SIMULATIONS

In this section, we will validate the accuracy of the proposed quasi-incompressible LBM, and compare it with a recent LBE model based on the incompressible phase-field theory given in [24] by a series of numerical simulations.

A. One-dimensional flat interface

We firstly validate the proposed LBE model by a flat interface test. Initially, the central region ($25 \leq y \leq 75$) is filled with fluid A and the rest is occupied by fluid B. The order parameter and density profiles are respectively set to be at equilibrium, i.e.,

$$\phi_0(y) = \begin{cases} \frac{\phi_A + \phi_B}{2} + \frac{\phi_A - \phi_B}{2} \tanh y_1, & y \leq 50 \\ \frac{\phi_A + \phi_B}{2} - \frac{\phi_A - \phi_B}{2} \tanh y_2, & y > 50 \end{cases} \quad (37)$$

$$\rho_0(y) = \begin{cases} \frac{\rho_A + \rho_B}{2} + \frac{\rho_A - \rho_B}{2} \tanh y_1, & y \leq 50 \\ \frac{\rho_A + \rho_B}{2} - \frac{\rho_A - \rho_B}{2} \tanh y_2, & y > 50 \end{cases} \quad (38)$$

where $y_1 = 2(y - 25)/W$ and $y_2 = 2(y - 75)/W$. The lattice used is $N_x \times N_y = 10 \times 100$ and periodic boundary conditions are employed in both x and y directions. The other parameters are fixed as $\rho_A = 1$, $\rho_B = 0.2$, $\tau_f = 1$, $\tau_g = 1$, $\phi_A = 1$, $\phi_B = 0$ and $\sigma = 0.001$. The effects of Pe and Cn numbers on the density distributions are investigated. Note that the characteristic length and velocity in this paper take the values of lattice space δx and velocity c , respectively. Figure 1 shows the density distribution across the interface for the quasi-incompressible (Quasi) model. From the figure, it can be seen that the density profiles match the analytical profile which indicates the accuracy of the proposed model in the interface tracking.

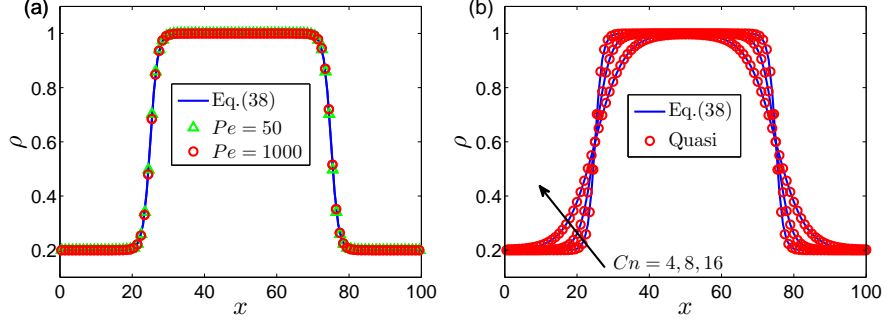


FIG. 1. (Color online) Density profiles across the interface with (a) different values of Pe with $Cn = 4$, and (b) different values of Cn with $Pe = 1000$.

B. Stationary droplet

A 2D stationary droplet problem is further tested to verify the present model. Initially, a circular droplet with radius ranging from 20 to 40 is placed in the middle of the computational domain with $N_x \times N_y = 100 \times 100$. The initial order parameter and density fields profile are given by

$$\phi_0(x, y) = \frac{\phi_A + \phi_B}{2} + \frac{\phi_A - \phi_B}{2} \tanh \left(2 \frac{R - \sqrt{(x - x_c)^2 + (y - y_c)^2}}{W} \right), \quad (39)$$

$$\rho_0(x, y) = \frac{\rho_A + \rho_B}{2} + \frac{\rho_A - \rho_B}{2} \tanh \left(2 \frac{R - \sqrt{(x - x_c)^2 + (y - y_c)^2}}{W} \right), \quad (40)$$

where (x_c, y_c) is the center of the droplet. Different values of Pe and Cn are respectively investigated. The other parameters are fixed as $\rho_A = 1$, $\rho_B = 0.2$, $\tau_f = 1$, $\tau_g = 1$, $\phi_A = 1$, $\phi_B = 0$ and $\sigma = 0.001$. When the droplet reaches the equilibrium state, the pressure difference ΔP between the inside and outside droplet should satisfy the Laplace law, i.e., $\Delta P = \sigma/R$, where P is calculated by $P = p_0 - \kappa \phi \nabla^2 \phi + \kappa |\nabla \phi|^2 / 2 + p$ with the equation of state $p_0 = \phi \partial_\phi \psi - \psi$ [23, 25]. Therefore, the surface tension can be calculated by $\sigma_{LBM} = R \Delta P$, and the numerical predictions and theoretical values of the surface tension are shown in Table I. It can be seen that the present quasi-incompressible LBE model satisfies the Laplace law. The distributions of the order parameter predicted by the both LBE models are shown in Fig. 2, and no obvious difference can be observed. In order to observe the distinctions between them, a moving interface problem is attempted to be simulated in the next section.

TABLE I. Numerical and theoretical values of surface tension with different Pe and Cn .

Surface tension	$Pe (Cn = 4)$			$Cn (Pe = 200)$		
	50	125	200	4	6	8
Numerical ($\times 10^{-3}$)	0.992	0.992	0.992	0.992	0.993	0.989
Theoretical ($\times 10^{-3}$)	1	1	1	1	1	1

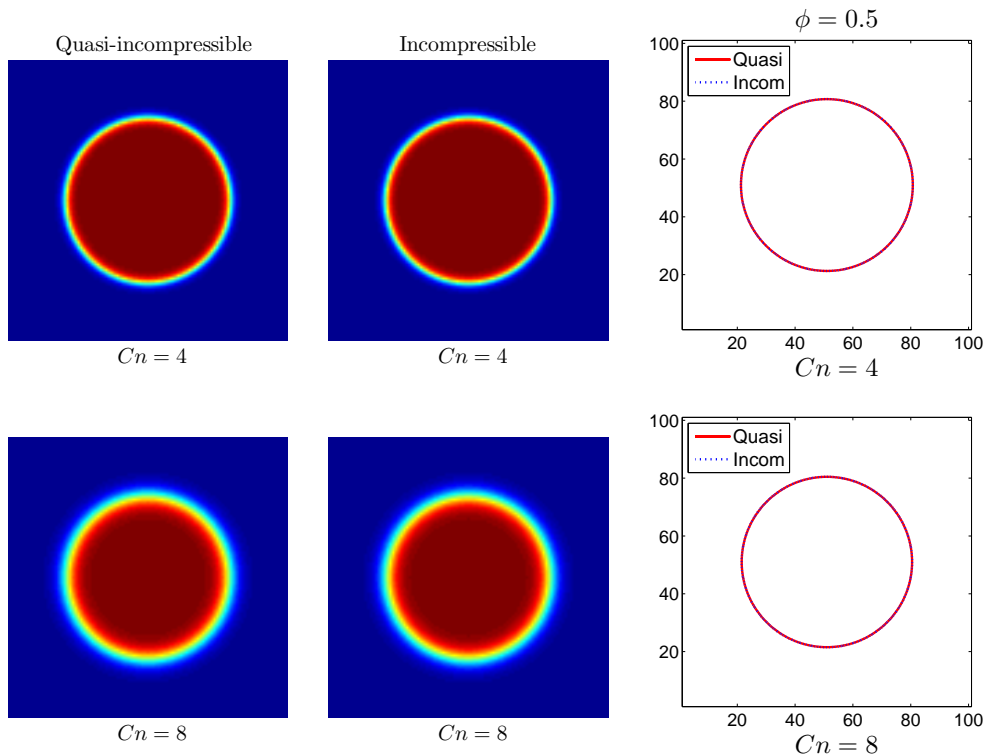


FIG. 2. (Color online) Order parameter configurations under different values of Cn with $Pe = 200$ fixed for the quasi-incompressible (Quasi) and incompressible (Incom) LBE models.

C. Bubble rising under buoyancy

In this section, a bubble rising under buoyancy is simulated to compare the two LBE models. Initially, a light circular bubble (fluid B) with radius R is immersed in another fluid (A) with higher density. To generate the buoyancy effect, a body force, $F_{b,y} = -(\rho - \rho_A)g$, is added to the fluid flow, where g is the gravitational acceleration. In the simulations, the computational domain is set to be 160×480 , and periodic boundary conditions are applied to all boundaries. The other parameters are set as follows: $\rho_A = 1$, $\rho_B = 0.5$, $g = 10^{-5}$, $\phi_A = 1$,

$\phi_B = 0$, $\tau_f = 1$, $\tau_g = 1$, $\sigma = 0.001$, $R = 32$, $Pe = 50$ and $Cn = 4$. Figure 3 shows the shape of the rising bubble at different times predicted by the two LBE models. It can be seen that the results are quite similar. A comparison of the interface shapes at $t = 10^4$ and 4×10^4 confirms the similarity in Fig. 4. Figure 5 shows the distributions of the dynamic pressure at different times, and the difference in the vicinity of the interface is more obvious. Figures 6 to 8 show the bubble velocity and the normalized velocity differences between the two LBE models. It can be seen from Figs. 6 and 7, the horizontal and vertical velocity components are nearly identical, but from Fig. 8, we can observe some the normalized velocity differences with maximum magnitude of order 10^{-2} . Based on the above observations, we can conclude that the predictions by the two LBE models yield almost the same results for this test case. According to the previous theoretical analysis, these phenomena are reasonable since the initial equilibrium order parameter yields the approximate uniform chemical potential so that the term $\gamma\phi\nabla \cdot (\lambda\nabla\mu)$ exerts a weak influence on the results.

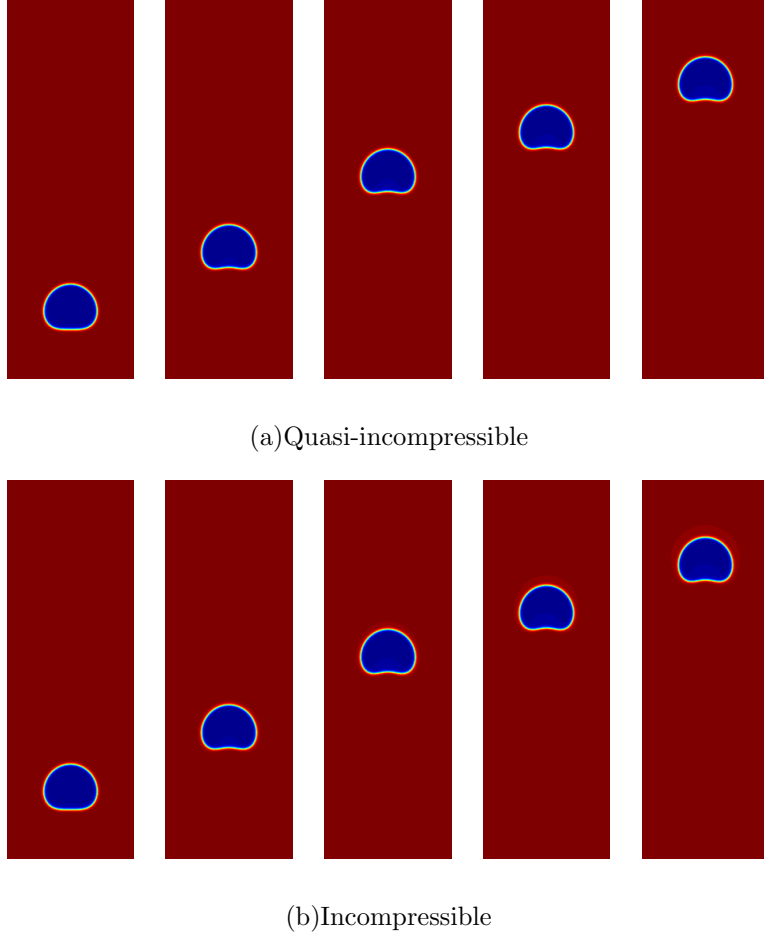


FIG. 3. (Color online) Density configuration of the rising bubble at $t/1000 = 10, 20, 30, 35, 40$ for the quasi-incompressible model (a) and incompressible model (b).

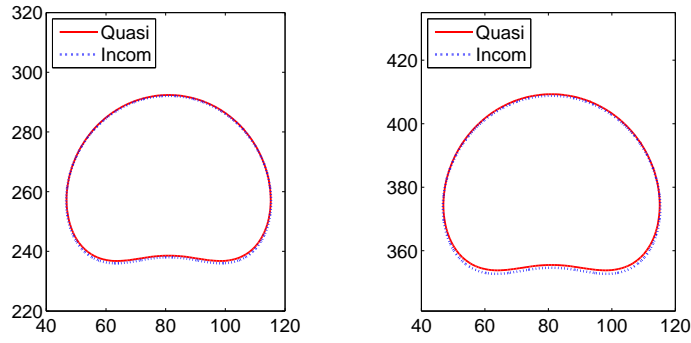


FIG. 4. (Color online) Density profiles predicted by the quasi-incompressible (Quais) and incompressible (Incom) LBE models at $t/1000 = 30, 40$.

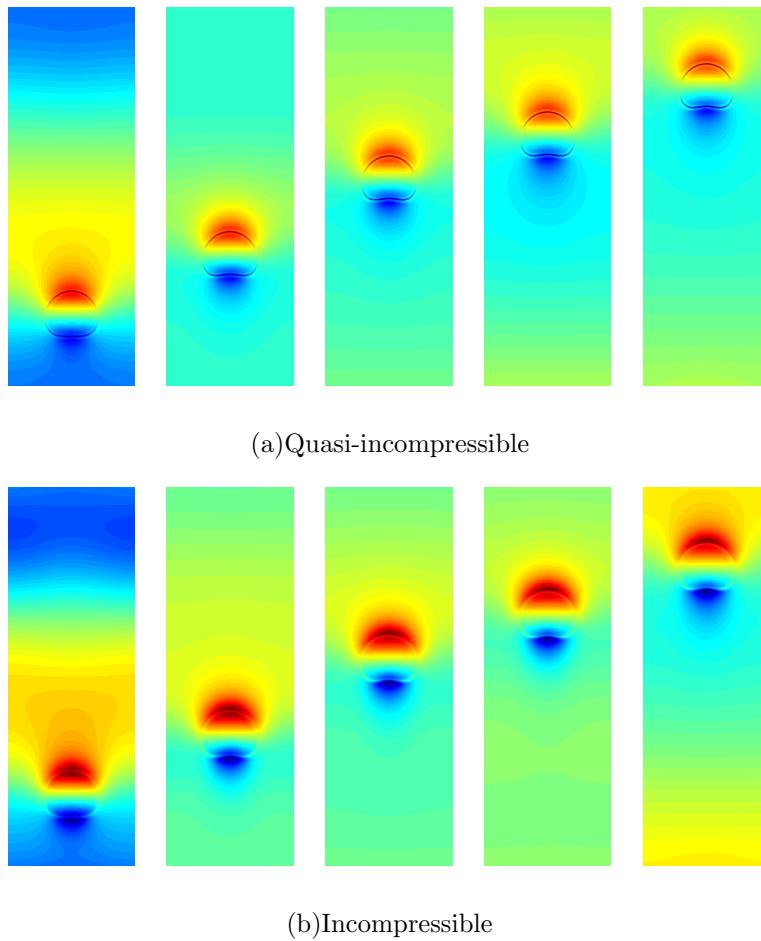
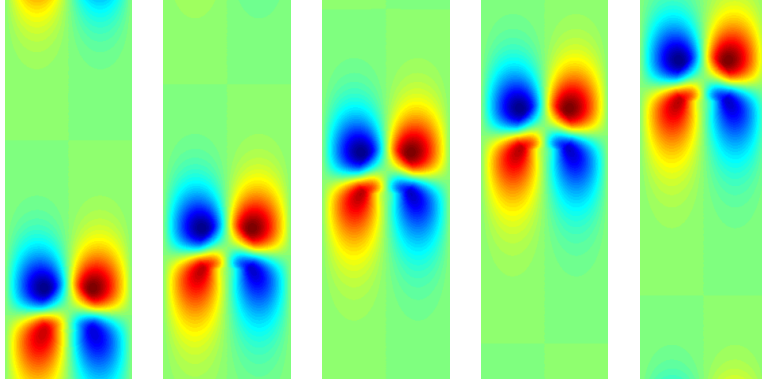
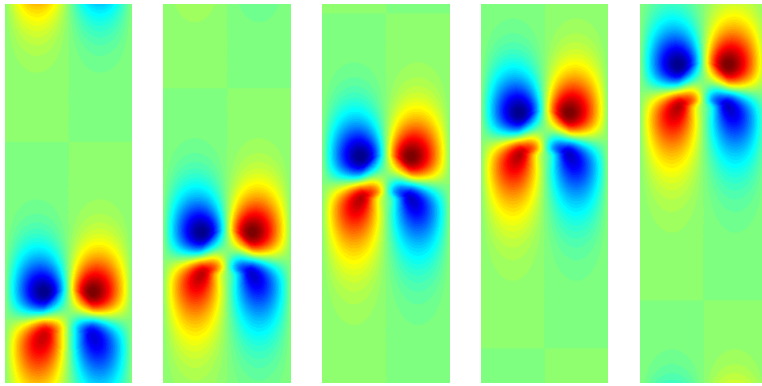


FIG. 5. (Color online) Dynamic pressure field of the rising bubble at $t/1000 = 10, 20, 30, 35, 40$ for the quasi-incompressible model (a) and incompressible model (b).

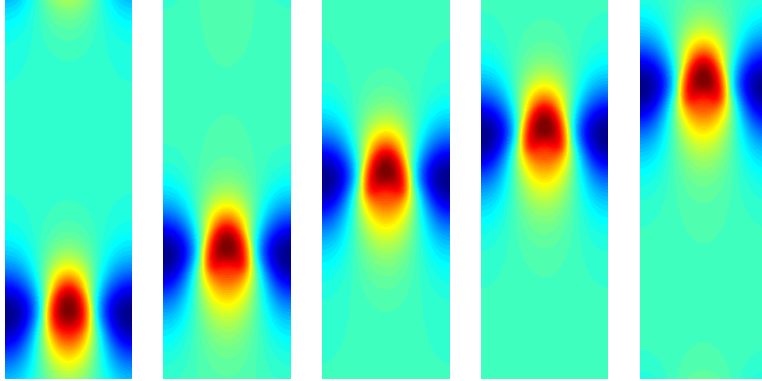


(a) Quasi-incompressible

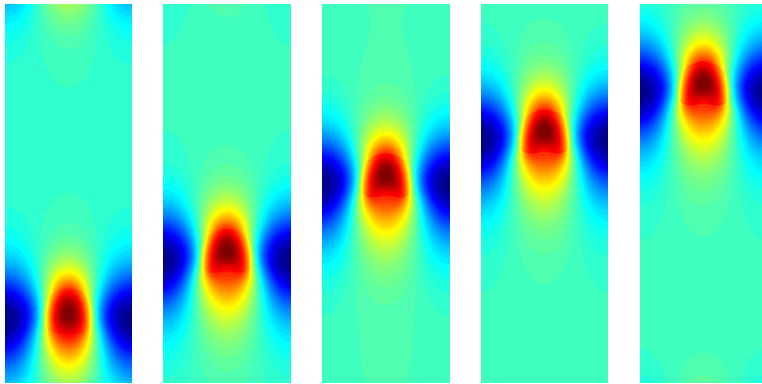


(b) Incompressible

FIG. 6. (Color online) Horizontal velocity of the rising bubble at $t/1000 = 10, 20, 30, 35, 40$ for the quasi-incompressible model (a) and incompressible model (b).



(a) Quasi-incompressible



(b) Incompressible

FIG. 7. (Color online) Vertical velocity of the rising bubble at $t/1000 = 10, 20, 30, 35, 40$ for the quasi-incompressible model (a) and incompressible model (b).

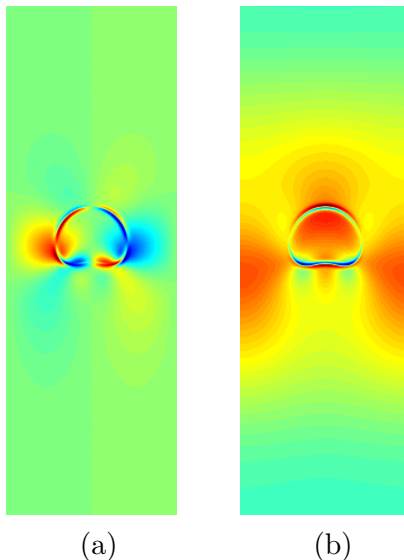


FIG. 8. Normalized velocity difference between the quasi-incompressible (Quais) model and incompressible (Incom) model at $t = 3 \times 10^4$, i.e, (a) $(u_{\text{Quasi}} - u_{\text{Incom}})/u_{\text{max,Quasi}}$ and (b) $(v_{\text{Quasi}} - v_{\text{Incom}})/v_{\text{max,Quasi}}$, where u_i and v_i are the horizontal and vertical velocities of model i , respectively, and $u_{\text{max,Quasi}}$ and $v_{\text{max,Quasi}}$ are the maximum horizontal and vertical velocities of quasi-incompressible model, respectively.

D. Phase separation

In this subsection, the simulation of phase separation will be carried out to further compare the two LBE models. Initially, the order parameter with a small perturbation is set as $\phi = 0.5[1 + 0.1\sin(4\pi x/Lx)\cos(4\pi y/Ly)]$, where x, y represent the Cartesian coordinates, and Lx and Ly are the length and width of the computational domain, respectively. To consider the effects of Pe, Cn and γ on the phase separation, different mobilities ($\lambda\beta = 0.02$ and 0.005), interfacial thicknesses ($W = 4$ and 8) and density ratios ($\rho_r = 2$ and 5) are taken into account in the simulations. The computational domain is set to be 100×100 . The other parameters are set as $\rho_A = 1, \phi_A = 1, \phi_B = 0, \tau_f = 1, \tau_g = 1$ and $\sigma = 0.001$. Periodic boundary conditions are applied to the all boundaries.

Figures 9 to 15 depict the density, dynamic pressure and velocity of the mixture with various dimensionless parameters γ, Pe and Cn . Firstly, we investigate the effect of γ as shown in Figs. 9 to 13. As $\gamma = 1$ (see Figs. 9 to 12), in the transient period, the density, pressure and velocity fields predicted by the two models are quite different. In the steady

state, although the density fields appears to be similar, the dynamic pressure and velocities are remarkably distinct. As $\gamma = 4$ (see Fig. 13), the density fields predicted by the two LBE models are opposite in the steady state, and the phase separation predicted by the present LBE model occurs earlier than that by the incompressible model. By comparing the Figs. 9 and 13, it can also be found that the density field from the present model varies with γ while that from the incompressible model does not. Then we further consider the effect of Peclet number. As Pe increases to 200 (see Fig. 14), it can be found the phase separation processes predicted by the two LBE models are both slowed down, but the distributions of the density fields are in opposite in the steady state. The effect of Cn on the phase separation process is also investigated. As shown in Fig. 15, when the Cn is increased from 4 to 8, the density fields change greatly. In the transient period ($t = 10^4$ to 9×10^4), the results predicted by the two LBE models present similar configurations; while in the steady state, some strips with different angles of inclination appear in the density fields. The above phenomena completely exhibit the discrepancy between the two models when the chemical potential is nonuniformly distributed due to the non-equilibrium order parameter, and the discrepancy is deeply influenced by the dimensionless parameters γ , Pe and Cn .

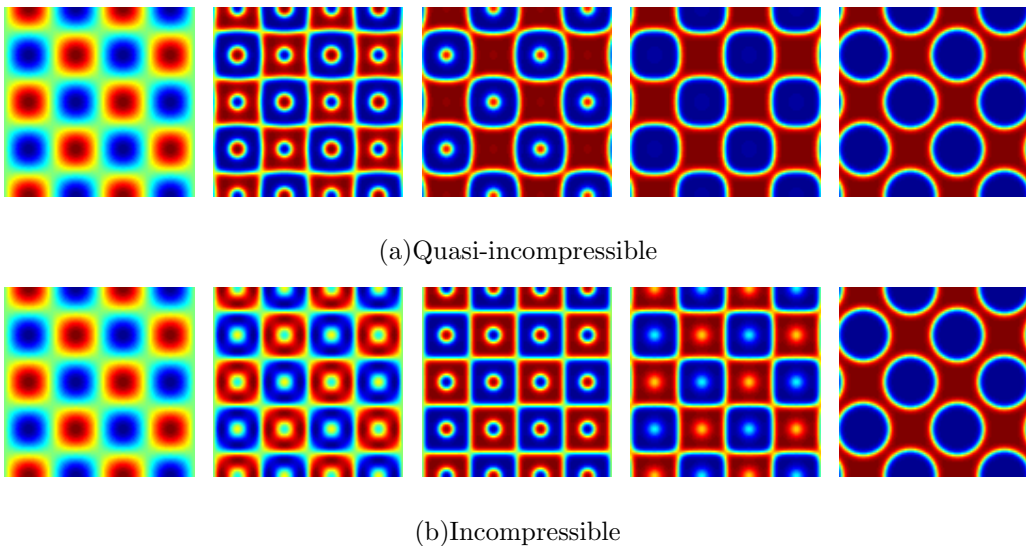
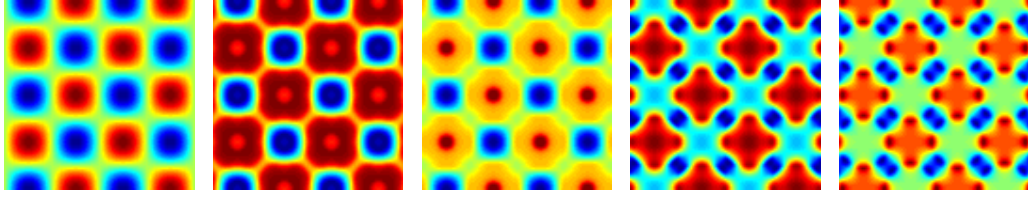
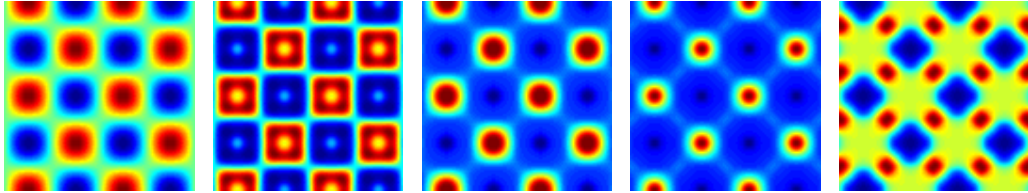


FIG. 9. (Color online) Density configuration with the minimum in blue and the maximum in red at $t/1000 = 0.1, 3, 5, 7, 20$ for the quasi-incompressible model (a) and incompressible model (b) as $\gamma = 1$, $Pe = 50$, and $Cn = 4$.

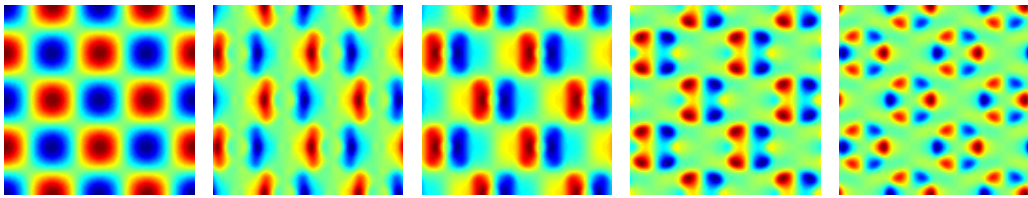


(a) Quasi-incompressible

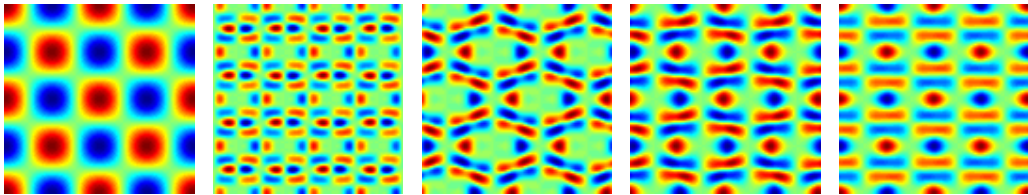


(b) Incompressible

FIG. 10. (Color online) Dynamic pressure field with the minimum in blue and the maximum in red at $t/1000 = 0.1, 3, 5, 7, 20$ for the quasi-incompressible model (a) and incompressible model (b) as $\gamma = 1$, $Pe = 50$, and $Cn = 4$.

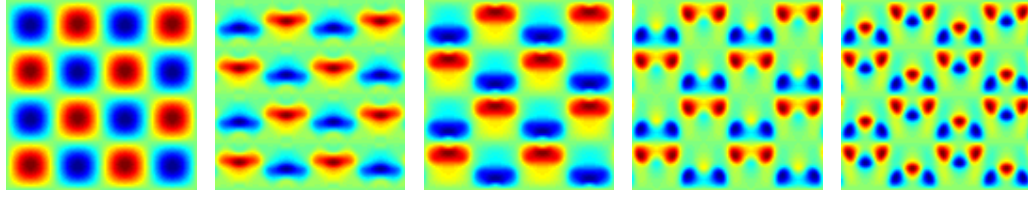


(a) Quasi-incompressible

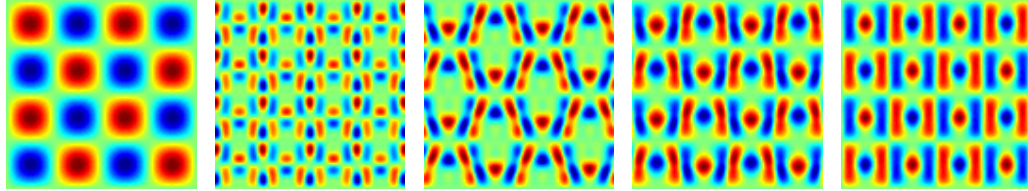


(b) Incompressible

FIG. 11. (Color online) Horizontal velocity with the minimum in blue and the maximum in red at $t/1000 = 0.1, 3, 5, 7, 20$ for the quasi-incompressible model (a) and incompressible model (b) as $\gamma = 1$, $Pe = 50$, and $Cn = 4$.

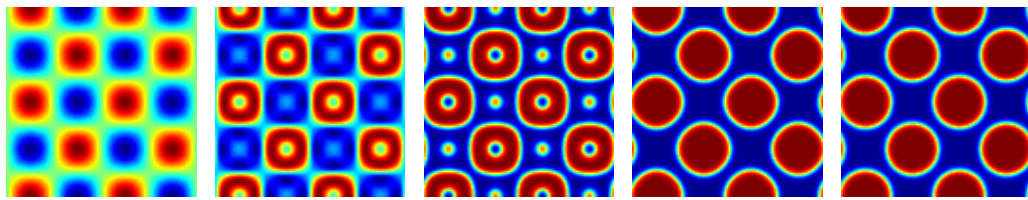


(a) Quasi-incompressible

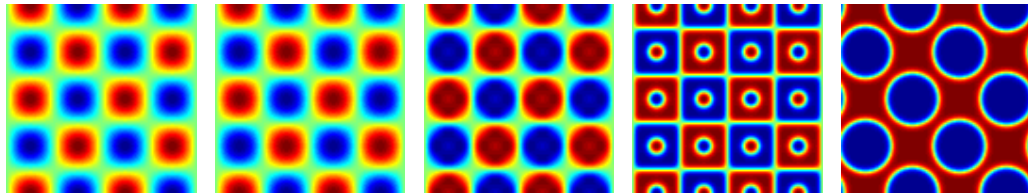


(b) Incompressible

FIG. 12. (Color online) Vertical velocity with the minimum in blue and the maximum in red at $t/1000 = 0.1, 3, 5, 7, 20$ for the quasi-incompressible model (a) and incompressible model (b) as $\gamma = 1$, $Pe = 50$, and $Cn = 4$.

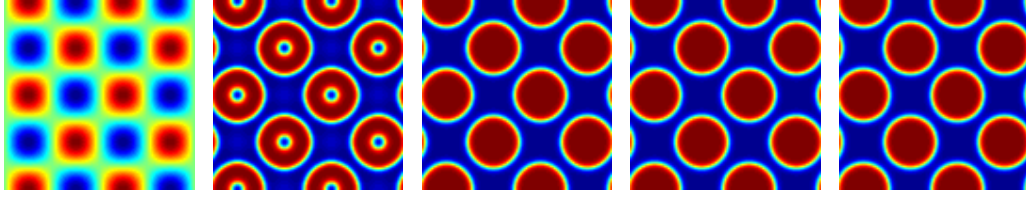


(a) Quasi-incompressible

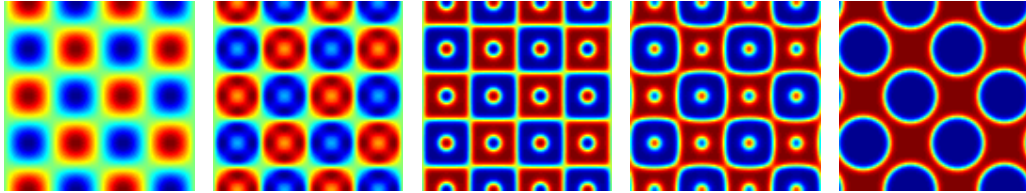


(b) Incompressible

FIG. 13. (Color online) Density configuration with the minimum in blue and the maximum in red at $t/1000 = 0.1, 1, 2, 4, 15$ for the quasi-incompressible model (a) and incompressible model (b) as $\gamma = 4$, $Pe = 50$, and $Cn = 4$.

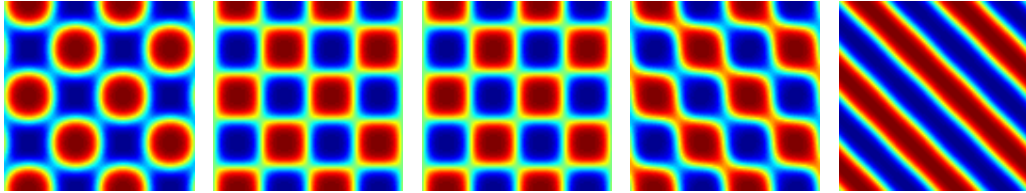


(a) Quasi-incompressible

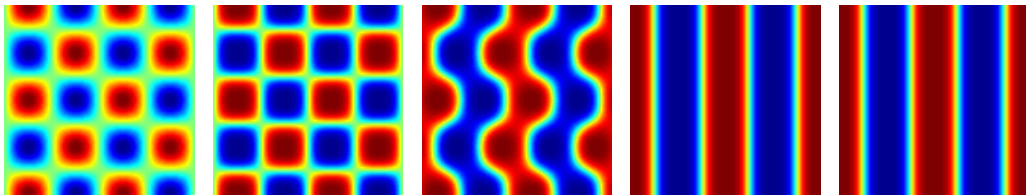


(b) Incompressible

FIG. 14. (Color online) Density configuration with the minimum in blue and the maximum in red at $t/1000 = 0.1, 10, 20, 25, 50$ for the quasi-incompressible model (a) and incompressible model (b) as $\gamma = 4$, $Pe = 200$, and $Cn = 4$.



(a) Quasi-incompressible



(b) Incompressible

FIG. 15. (Color online) Density configuration with the minimum in blue and the maximum in red at $t/1000 = 10, 60, 90, 200, 240$ for the quasi-incompressible model (a) and incompressible model (b) as $\gamma = 4$, $Pe = 200$, and $Cn = 8$.

V. CONCLUSIONS

In this study, a LBE model for binary fluids is proposed based on the quasi-incompressible phase-field theory, which overcomes the mass conservation problem in the incompressible

phase-field LBM. To validate the accuracy of the proposed model and compare its performance with an incompressible model, a series of numerical tests are performed.

Firstly, with the one-dimensional flat interface and stationary droplet tests, it is shown that the proposed LBE model can track the interface accurately and satisfies the Laplace law. Furthermore, the comparison of the stationary droplet shows no obvious difference between the two LBE model. Then, the test of the bubble rising under buoyancy shows that some subtle distinctions exist in the two LBE models but overall they still agree with each other qualitatively. The results of the phase separation problem show the dynamic processes and static structures from the two models can be rather different. These phenomena indicate that there are some distinctions between the two models involved with the multiphase flows, especially for problems with the nonuniform distribution of chemical potential. Since the quasi-incompressible LBE model satisfies the fundamental mass conservation law, its results should be more reliable.

ACKNOWLEDGMENT

This study is financially supported by the National Natural Science Foundation of China. (Grant No. 51125024).

APPENDIX: CHAPMAN-ENSKOG ANALYSIS OF THE QUASI-INCOMPRESSIBLE LBE MODEL

In this section, the proposed LBE model for hydrodynamic equations is firstly analyzed by applying the Chapman-Enskog expansion

$$f_i = f_i^{(0)} + \varepsilon f_i^{(1)} + \varepsilon^2 f_i^{(2)} + \dots \quad (41)$$

$$\partial_t = \varepsilon \partial_{t_0} + \varepsilon^2 \partial_{t_1}, \quad \nabla = \varepsilon \nabla_0, \quad F_i = \varepsilon F_i^{(0)} + \varepsilon^2 F_i^{(1)}, \quad (42)$$

with

$$F_i^{(0)} = (\mathbf{c}_i - \mathbf{u}) \cdot [\omega_i \Gamma_i \mathbf{F} + \omega_i s_i c_s^2 \nabla \rho], \quad F_i^{(1)} = -\omega_i c_s^2 \rho \gamma \nabla \cdot (\lambda \nabla \mu), \quad (43)$$

where ε is a small expansion parameter. Using the Taylor expansion in Eq. (22), one can obtain

$$D_i f_i + \frac{\delta t}{2} D_i^2 f_i = -\frac{1}{\tau_c} (f_i - f_i^{eq}) + \left(1 - \frac{1}{2\tau_f}\right) F_i, \quad (44)$$

where $\tau_c = \tau_f \delta t$, and $D_i = \partial_t + \mathbf{c}_i \cdot \nabla$. The substitution of Eqs. (41) and (42) into Eq. (44) yields the Chapman-Enskog system as

$$O(\varepsilon^0) : f_i^{(0)} = f_i^{eq}, \quad (45)$$

$$O(\varepsilon^1) : D_{0i} f_i^{(0)} - \left(1 - \frac{1}{2\tau_f}\right) F_i^{(0)} = -\frac{1}{\tau_c} f_i^{(1)}, \quad (46)$$

$$O(\varepsilon^2) : \partial_{t_1} f_i^{(0)} + D_{0i} f_i^{(1)} + \frac{\delta t}{2} D_{0i}^2 f_i^{(0)} = -\frac{1}{\tau_c} f_i^{(2)} + \left(1 - \frac{1}{2\tau_f}\right) F_i^{(1)}. \quad (47)$$

Then, the substitution of Eq. (46) into (47) yields

$$\partial_{t_1} f_i^{(0)} + \left(1 - \frac{1}{2\tau_f}\right) D_{0i} f_i^{(1)} + \frac{\delta t}{2} \left(1 - \frac{1}{2\tau_f}\right) D_{0i} F_i^{(0)} = -\frac{1}{\tau_c} f_i^{(2)} + \left(1 - \frac{1}{2\tau_f}\right) F_i^{(1)}. \quad (48)$$

Meanwhile, from the definitions (24) and (43), it is easy to calculate the following moments:

$$\sum_i f_i^{eq} = p, \quad \sum_i c_i f_i^{eq} = c_s^2 \rho \mathbf{u}, \quad (49)$$

$$\sum_i c_i c_i f_i^{eq} = c_s^2 p + c_s^2 \rho \mathbf{u} \mathbf{u}, \quad (50)$$

$$\sum_i c_i c_i c_i f_i^{eq} = c_s^4 \rho (u_\alpha \delta_{\beta\gamma} + u_\beta \delta_{\alpha\gamma} + u_\gamma \delta_{\alpha\beta}), \quad (51)$$

$$\sum_i F_i^{(0)} = c_s^2 \mathbf{u} \cdot \nabla \rho, \quad \sum_i F_i^{(1)} = -c_s^2 \rho \gamma \nabla \cdot (\lambda \nabla \mu), \quad (52)$$

$$\sum_i \mathbf{c}_i F_i^{(0)} = c_s^2 \mathbf{F}, \quad \sum_i \mathbf{c}_i F_i^{(1)} = 0, \quad (53)$$

$$\sum_i c_i c_i F_i^{(0)} = c_s^2 (\mathbf{F}' \mathbf{u} + \mathbf{u} \mathbf{F}') + c_s^4 \mathbf{u} \cdot \nabla \rho, \quad \sum_i c_i c_i F_i^{(1)} = -c_s^4 \rho \gamma \nabla \cdot (\lambda \nabla \mu), \quad (54)$$

where $\mathbf{F}' = \mathbf{F} + c_s^2 \nabla \rho$. From Eqs. (31), (32) and (49), we can obtain

$$\sum_i f_i^{(1)} = -\frac{\delta t}{2} c_s^2 \mathbf{u} \cdot \nabla \rho, \quad \sum_i f_i^{(2)} = \frac{\delta t}{2} c_s^2 \gamma \rho \nabla \cdot (\lambda \nabla \mu), \quad \sum_i f_i^{(k)} = 0, \quad k > 2 \quad (55)$$

$$\sum_i c_i f_i^{(1)} = -\frac{\delta t}{2} c_s^2 \mathbf{F}, \quad \sum_i c_i f_i^{(k)} = 0, \quad k > 1 \quad (56)$$

Taking the zeroth- and first-order moments of Eq. (46), we can obtain

$$\frac{1}{\rho c_s^2} \partial_{t_0} p + \nabla \cdot \mathbf{u} = 0, \quad (57)$$

$$\partial_{t_0} (\rho \mathbf{u}) + \nabla \cdot (p + \rho \mathbf{u} \mathbf{u}) = \mathbf{F}. \quad (58)$$

Likewise, taking the zeroth- and first-order moments of Eq. (48), we can obtain

$$\partial_{t_1} p = -c_s^2 \rho \gamma \nabla \cdot (\lambda \nabla \mu), \quad (59)$$

$$\partial_{t_1}(c_s^2 \rho \mathbf{u}) + \nabla_0 \cdot \left[\left(1 - \frac{1}{2\tau_f} \right) \sum_i \mathbf{c}_i \mathbf{c}_i f_i^{(1)} \right] + \frac{\delta t}{2} \nabla_0 \cdot \left[\left(1 - \frac{1}{2\tau_f} \right) \sum_i \mathbf{c}_i \mathbf{c}_i F_i^{(0)} \right] = 0. \quad (60)$$

According to the Eqs. (46), and (57) to (59),

$$\begin{aligned} -\frac{1}{\tau_c} \sum_i \mathbf{c}_i \mathbf{c}_i f_i^{(1)} &= c_s^4 \mathbf{u} \cdot \nabla \rho + c_s^2 (\mathbf{u} \mathbf{F}' + \mathbf{F}' \mathbf{u}) + c_s^4 \rho (\nabla \mathbf{u} + \nabla \mathbf{u}^T) \\ &\quad - \sum_i \left(1 - \frac{1}{2\tau_f} \right) \mathbf{c}_i \mathbf{c}_i F_i^{(0)} + O(M_a^3). \end{aligned} \quad (61)$$

Substituting Eq. (61) into Eq. (60), we can obtain

$$\partial_{t_1}(\rho \mathbf{u}) = \nabla \cdot [\rho \nu (\nabla \mathbf{u} + \nabla \mathbf{u}^T)], \quad (62)$$

where $\nu = c_s^2(\tau_f - 0.5)\delta t$. From Eqs. (57) and (59), we can obtain the continuity equation

$$\frac{1}{\rho c_s^2} \partial_t p + \nabla \cdot \mathbf{u} = -\gamma \nabla \cdot (\lambda \nabla \mu). \quad (63)$$

Similarly, the momentum equation can be derived from Eqs. (58) and (62)

$$\partial_t(\rho \mathbf{u}) + \nabla \cdot (\rho \mathbf{u} \mathbf{u}) = -\nabla p + \nabla \cdot [\rho \nu (\nabla \mathbf{u} + \nabla \mathbf{u}^T)] + \mathbf{F}. \quad (64)$$

Next we will derive the CH equation from Eq. (23) by the Chapman-Enskog expansion. Similarly, the multiscale expansions are given by

$$\mathbf{g}_i = \mathbf{g}_i^{(0)} + \varepsilon \mathbf{g}_i^{(1)} + \varepsilon^2 \mathbf{g}_i^{(2)} + \dots, \quad (65)$$

$$\partial_t = \varepsilon \partial_{t_0} + \varepsilon^2 \partial_{t_1}, \quad \nabla = \varepsilon \nabla_0, \quad G_i = \varepsilon G_i^{(0)}. \quad (66)$$

Using the Taylor expansion in Eq. (23), one can obtain

$$D_i \mathbf{g}_i + \frac{\delta t}{2} D_i^2 \mathbf{g}_i = -\frac{1}{\tau_c} (\mathbf{g}_i - \mathbf{g}_i^{eq}) + \left(1 - \frac{1}{2\tau_g} \right) G_i, \quad (67)$$

where $\tau_c = \tau_g \delta t$. Substituting Eqs. (65) and (66) into the Eq. (67), we can obtain the following infinite consecutive series of equations

$$O(\varepsilon^0) : \quad \mathbf{g}_i^{(0)} = \mathbf{g}_i^{eq}, \quad (68)$$

$$O(\varepsilon^1) : \quad D_{0i} \mathbf{g}_i^{(0)} - \left(1 - \frac{1}{2\tau_g} \right) G_i^{(0)} = -\frac{1}{\tau_c} \mathbf{g}_i^{(1)}, \quad (69)$$

$$O(\varepsilon^2) : \quad \partial_{t_1} \mathbf{g}_i^{(0)} + D_{0i} \mathbf{g}_i^{(1)} + \frac{\delta t}{2} D_{0i}^2 \mathbf{g}_i^{(0)} = -\frac{1}{\tau_c} \mathbf{g}_i^{(2)}. \quad (70)$$

Then substituting Eq. (69) into Eq. (70), we can obtain

$$\partial_{t_1} \mathbf{g}_i^{(0)} + \left(\tau_c - \frac{\delta t}{2} \right) D_{0i} G_i^{(0)} + \left(\frac{\delta t}{2} - \tau_c \right) D_{0i}^2 \mathbf{g}_i^{(0)} = -\frac{1}{\tau_c} \mathbf{g}_i^{(2)}. \quad (71)$$

In order to recover the CH equation, we derive the following moments from the Eq. (25) and Eq. (29),

$$\sum_i g_i^{eq} = \phi, \quad \sum_i c_i g_i^{eq} = \phi \mathbf{u}, \quad \sum_i c_i c_i g_i^{eq} = \phi \mathbf{u} \mathbf{u} + \mathbf{c}_s^2 \alpha \mu, \quad (72)$$

$$\sum_i G_i = 0, \quad \sum_i \mathbf{c}_i G_i = \frac{\phi}{\rho} \mathbf{G}, \quad (73)$$

where $\mathbf{G} = -\nabla p + \mathbf{F}$. Taking the zeroth-order moment of Eqs. (69) and (71), we can obtain

$$\partial_{t_0} \phi + \nabla \cdot (\phi \mathbf{u}) = 0, \quad (74)$$

$$\partial_{t_1} \phi + \left(\frac{\delta t}{2} - \tau_c \right) \left[\partial_{t_0}^2 \phi + 2 \partial_{t_0} \nabla \cdot (\phi \mathbf{u}) + \nabla \cdot \nabla \cdot (\phi \mathbf{u} \mathbf{u} + \mathbf{c}_s^2 \alpha \mu) - \nabla \cdot \left(\frac{\phi}{\rho} \mathbf{G} \right) \right] = 0. \quad (75)$$

According to Eqs. (58) and (74), the Eq. (75) reduces to the following equation

$$\partial_{t_1} \phi = \lambda \nabla^2 \mu, \quad (76)$$

where $\lambda = c_s^2 \alpha \delta t (\tau_g - 1/2)$. Combined Eqs. (74) and (76), we can obtain the CH equation as follows

$$\partial_t \phi + \nabla \cdot (\phi \mathbf{u}) = \lambda \nabla^2 \mu. \quad (77)$$

From Eqs. (11), (63) and (77), we can derive the following mass conservation equation by neglecting the term $\partial_t p$, which is of order Ma^2

$$\partial_t \rho + \nabla \cdot (\rho \mathbf{u}) = 0, \quad (78)$$

and then the momentum equation in Eq. (64) could be rewritten as

$$\rho \left(\frac{\partial \mathbf{u}}{\partial t} + \mathbf{u} \cdot \nabla \mathbf{u} \right) = -\nabla p + \nabla \cdot [\rho \nu (\nabla \mathbf{u} + \nabla \mathbf{u}^T)] + \mathbf{F}. \quad (79)$$

-
- [1] C. W. Hirt and B. D. Nichols, *J. Comput. Phys.* 39, 201 (1981).
 - [2] G. Tryggvason, B. Bunner, A. Esmaeeli, D. Juric, N. Al-Rawahi, W. Tauber, J. Han, S. Nas, Y. -J. Jan, *J. Comput. Phys.* 169, 708 (2001).
 - [3] M. Sussman, P. Smereka, S. Osher, *J. Comput. Phys.* 114, 146 (1994).
 - [4] L. Q. Chen, J. Shen, *Comput. Phys. Commun.* 108, 147 (1998).
 - [5] D. Jacqmin, *J. Comput. Phys.* 155, 96 (1999).
 - [6] H. Ding, P. D. Spelt, C. Shu, *J. Comput. Phys.* 226, 2078 (2007).

- [7] J. Shen, X. Yang, *SIAM J. Sci. Comput.* 32, 1159 (2010).
- [8] J. Lowengrub, L. Truskinovsky, *Proc. R. Soc. London, Ser. A* 454, 2617 (1998).
- [9] X. He, S. Chen, R. Zhang, *J. Comput. Phys.* 152, 642 (1999).
- [10] H. Zheng, C. Shu, Y. Chew, *Phys. Rev. E* 72, 056705 (2005).
- [11] T. Lee, C. -L. Lin, *J. Comput. Phys.* 206, 16 (2005).
- [12] F. Chen, J. Shen, *Commun. Comput. Phys.* 13, 1189 (2013).
- [13] C. Liu, J. Shen, *Physica D* 179, 211 (2002).
- [14] Z. Chen, R.H. Nochetto, A. Schmidt, *M2AN Math. Model. Numer. Anal.* 34, 775 (2000).
- [15] Q. Du, J. Zhang, *SIAM J. Sci. Comput.* 30, 1634, (2008).
- [16] X. Feng, *SIAM J. Numer. Anal.* 44, 1049 (2006).
- [17] D. Jacqmin, *J. Fluid Mech.* 402, 57 (2000).
- [18] P. Yue, J.J. Feng, C. Liu, J. Shen, *J. Fluid Mech.* 515, 293 (2004).
- [19] S. Chen and G.D. Doolen, *Annu. Rev. Fluid Mech.* 30, 329 (1998).
- [20] T. Lee, L. Liu, *J. Comput. Phys.* 229, 8045 (2010).
- [21] A. Fakhari, T. Lee, *Phys. Rev. E* 87, 023304 (2013).
- [22] H. Zheng, C. Shu, Y. -T. Chew, *J. Comput. Phys.* 218, 353 (2006).
- [23] Y. Zu, S. He, *Phys. Rev. E* 87, 043301 (2013).
- [24] H. Liang, B. Shi, Z. Guo, Z. Chai, *Phys. Rev. E* 89, 053320 (2014).
- [25] L. Zheng, S. Zheng, Q. Zhai, *Phys. Rev. E* 91, 013309 (2015).
- [26] Q. Li, K. Luo, Y. Gao, Y. He, *Phys. Rev. E* 85, 026704 (2012).
- [27] J. Shen, X. Yang, Q. Wang, *Comm. Comp. Phys.* 13, 1045 (2013).
- [28] D. Jacqmin, *J. Fluid Mech.* 402, 57 (2000).
- [29] Y. Yan, Y. Zu, *J. Comput. Phys.* 227, 763 (2007).
- [30] J. S. Rowlinson and B. Widom, *Molecular Theory of Capillarity* (Clarendon, Oxford, 1982).
- [31] J.W. Cahn, J.E. Hilliard, *J. Chem. Phys.* 28, 258 (1958).
- [32] J.W. Cahn, J.E. Hilliard, *J. Chem. Phys.* 31, 688 (1959).
- [33] V. Badalassi, H. Ceniceros, S. Banerjee, *J. Comput. Phys.* 190, 371 (2003).
- [34] Z. Chai, T. Zhao, *Phys. Rev. E* 87, 063309 (2013).
- [35] Z. Guo, C. Zheng, B. Shi, *Phys. Rev. E* 83, 036707 (2011).